JACS
JOURNAL OF THE AMERICAN CHEMICAL SOCIETY
Article
pubs.acs.org/JACS

Differentially Instructive Extracellular Protein Micro-nets

Nilofar Faruqui,[†,§] Angelo Bella,[†,§] Jascindra Ravi,[†] Santanu Ray,[†] Baptiste Lamarre,[†] and Maxim G. Ryadnov*[,†,‡]

[†]National Physical Laboratory, Hampton Road, Teddington TW11 0LW, U.K.
[‡]School of Physics and Astronomy, University of Edinburgh, Edinburgh EH9 3JZ, U.K.

Supporting Information

ABSTRACT: An ability to construct biological matter from the molecule up holds promise for applications ranging from smart materials to integrated biophysical models for synthetic biology. Biomolecular self-assembly is an efficient strategy for biomaterial construction which can be programmed to support desired function. A challenge remains in replicating the strategy synthetically, that is at will, and differentially, that is for a specific function at a given length scale. Here we introduce a self-assembly topology enabling a net-like architectural mimetic of native extracellular matrices capable of differential responses to cell adhesion—enhanced mammalian cell attachment and proliferation, and enhanced resistance to bacterial colonization—at the native sub-millimeter length scales. The biological performance of such protein micro-nets directly correlates with their morphological and chemical properties, offering thus an application model for differential extracellular matrices.

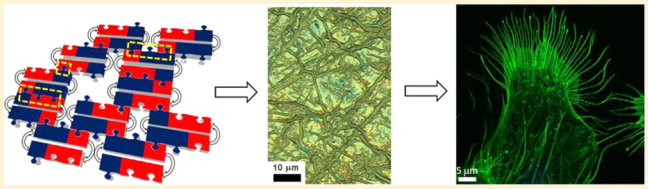

INTRODUCTION

Synthetic extracellular matrices are requisite for a variety of applications, and increasingly so for modern molecular medicine where novel materials that direct biology the way nature does are in steady demand.[1] Peptide self-assembly offers a particularly attractive strategy as it can mimic native designs from the bottom up.[2] Existing mimetics are anisotropic fibrillar structures characterized by unidirectional near-crystalline order,[3] which, though providing necessary control over fibrillogenesis, may limit topographical cues to nanometer scales.[4] By contrast, native extracellular matrices allow significant orthogonality in their assembly whereby generating multiscale fibrillar networks and meshes.[5] Although it is possible to render synthetic assemblies orthogonal with the help of co-assembling specialist blocks,[6] resulting morphologies span similar nanometer dimensions within which functional cell support may not be efficient. Indeed, rigidified nanoscale geometries cannot readily accommodate subtle morphological alterations that are inevitable in dynamic cellular environements.[7] They may confine such changes to sub-microscopic niches, which is sufficient for supporting local adhesive contacts promoting integrin-mediated attachments, but cannot support contiguous cellular recruitment across larger length scales.[8] Structurally adaptive strategies are devised to provide more efficient solutions and can be exemplified by biocatalytic induction[9] and pairwise axial interactions[10] to access higher ordered structures with a better control over assembly and stability or primary amphiphile displays having high densities of binding epitopes.[11] Such designs are typically supported by gelation, with their architectures, in contrast to the native matrices, being not necessarily characteristic of structurally persistent and regular networks having mesh sizes exceeding several micrometers.[8−11] DNA tile self-assembly,[12] which may help tackle the problem of mimicking protein fibrillogenesis, is not restricted to nanometer length scales[13] and can afford persistence lengths that can be tuned to support cell adhesion.[14] However, the question remains as to our ability to structurally program a non-gelated protein mimetic of the native matrices. This is the microscale architecture of protein matrices that ensures different biological functions ranging from cell adhesion[1,5] to mucosal innate immunity,[15] which are often expressed in combination. Therefore, the main emphasis should be on those synthetic mimetics that enable matrix architectures able to elicit differential biological responses at the microscopic length scales—a synthetic ability that has yet to emerge. Here we introduce a structural rationale for the programming of sub-millimeter matrix architectures which support adhesion, growth and proliferation of mammalian cells and efficiently resist bacterial colonization. The design is a single peptide block providing a self-assembly topology, which (i) is free of directionality constraints, (ii) spans microscopic dimensions, and (iii) is biologically differential.

RESULTS AND DISCUSSION

Peptide Design. The topology is a cyclized sequence of α-helical heptad repeats of polar (P) and hydrophobic (H) residues, PHPPHPP, derived from archetypal coiled-coil motifs.[16] Two complementary repeats, namely anionic EIAALEQ and cationic KIAALKQ,[17,18] arrange into an asymmetric pattern of two domains, each comprising three

Received: November 6, 2013
Published: May 13, 2014

dx.doi.org/10.1021/ja411325c | J. Am. Chem. Soc. 2014, 136, 7889−7898

heptads (Figure 1a,b and Table S1 and Scheme S1 in the Supporting Information).

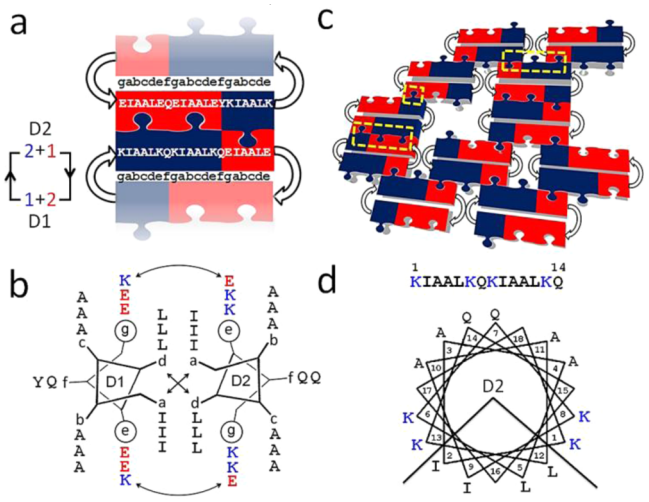

Figure 1. Peptide design. (a) Schematic representations of the SaNet topology with a 2+1 asymmetric pattern of the heptads in two domains, D1 and D2. One puzzle piece denotes one heptad. Heptad repeats designated *gabcdef* are shown above the linear sequences highlighted in the blocks. The arrows indicate the N-to-C directionality of the sequences. Each arrow is a triglycyl linker. (b) Domain sequences configured onto coiled-coil helical wheels with 3.5 residues per turn. Curved double-headed arrows indicate electrostatic interactions between *g* and *e*′ (circled); crossed arrows show a hydrophobic interface of a heterodimer favored by isoleucines and leucines in *a* and *d*, respectively; *b*, *c* and *f* are solvent-exposed and are small and neutral alanines and glutamines; a single *f* site is made tyrosine to allow concentration measurements using absorbance at 280 nm. (c) Simplified representation of the SaNet assembly with one-, two-, and three-heptad overlaps highlighted by dashed yellow lines. (d) The cationic stretch of D2 sequence configured onto an antimicrobial helical wheel with 3.6 residues per turn, showing the clustering of amino acid residues into two distinctive polar and hydrophobic faces. Blue and red denote cationic and anionic heptads and residues, respectively.

Domain 1 (D1) contains two anionic and one cationic heptads, whereas for domain 2 (D2) the arrangement is reverse. Such a split 2+1/1+2 pattern enables arbitrary interactions between the domains promoting various heptad overlaps (Figure 1c). Cyclisation renders the topology orthogonally closed making each of the overlaps probable in any direction with respect to the plane of the cycle. The orientation of the domains in the cyclopeptide is antiparallel which ensures interactions between different peptides and not within the same peptide. This is reinforced by two triglycyl linkers that fix domains at their termini favoring outward interactions (Figure 1a and Scheme S1). The resulting bifaceted block assembles through heptad overlaps or "knots" (Figure 1a,c). Three-heptad knots maintain continuous lateral assembly, which ensures fiber formation, while less stable one-heptad overlaps propagate longitudinally through cooperative two-heptad knots (Figure 1c). The overall assembly is thus indiscriminate and can redirect at any point. This is expected to yield mesoscopic net-like structures of fibers with broad width distributions. We refer to this topology as a self-assembling net (SaNet).

Assembly and Folding. Consistent with the design, confocal, optical, and atomic force microscopy (AFM) revealed irregular and densely knotted nets formed by relatively short intersecting fiber networks (Figures 2 and S1a,b). The structures extended tens of micrometers in length with fiber

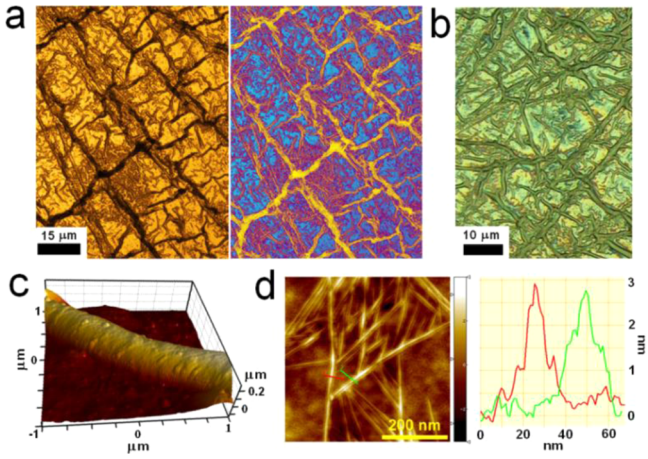

Figure 2. Peptide assembly. Confocal (a) and optical (b) micrographs of higher order networks. The color-inverted image (a) highlights clusters of lower order assemblies (purple). AFM topography images of a high-order fiber (c) and lower-order fibrillar branches with cross sections along the highlight lines (d). Assembly conditions: peptide (100 μM) incubated overnight at 20 °C in 10 mM MOPS buffer, pH 7.4.

thicknesses ranging from 200 nm to ~1 μm, which was in good agreement with size distributions obtained by dynamic light scattering measurements (Figures 2a–c, S1c, and S2a). Developing or lower-order networks, which were dominated by periodic branching and patching of growing branches (Figures 2d and S1d), were also observed.[6] AFM analyses of these lower order branches gave conservative thicknesses of ~3 nm suggesting a lateral packing of the folded peptide blocks along the fiber axis (Figure 2d).

The SaNet block is of a 2 × 3 nm rod-shaped mesogen, in which the cyclic backbone, which rigidifies upon folding, is likely to provide a near-crystalline order through cooperative three-heptad knot interactions, when complementary helices are fully aligned with all electrostatic interactions satisfied, and staggered knot interactions, when only some interhelical interactions are satisfied, which provide a network-like propagation (Figure 1c).[19] Small fibers of 10 nm widths may account for the side-by-side assembly of 2 nm thick protofillaments, which upon organizing into higher order assemblies entangle through branching patches[6] with the formation of arbitrary net points. The persistence length of higher order fibers was high, so was the rate and frequency with which branching was generated.

Therefore, the assembly might undergo through two independent but synergistic processes including persistent nucleation of branching and a homeotropic stack-like alignment of the cyclopeptide blocks in a fashion similar to that of amyloid assemblies.[20]

Additionally, in some cases fiber networks tended to associate with clusters of pool-like assemblies that were also rich in low order branching (Figure 2a). Consistent with these observations, control mixtures of individual D1 and D2 (D1+D2), which in principle can form three-heptad interactions and build upon each other, did not propagate (Figure S1e,f). To assemble, these blocks have to be in register, which, in contrast to the SaNet, is compromised by competitive

dx.doi.org/10.1021/ja411325c | J. Am. Chem. Soc. 2014, 136, 7889–7898

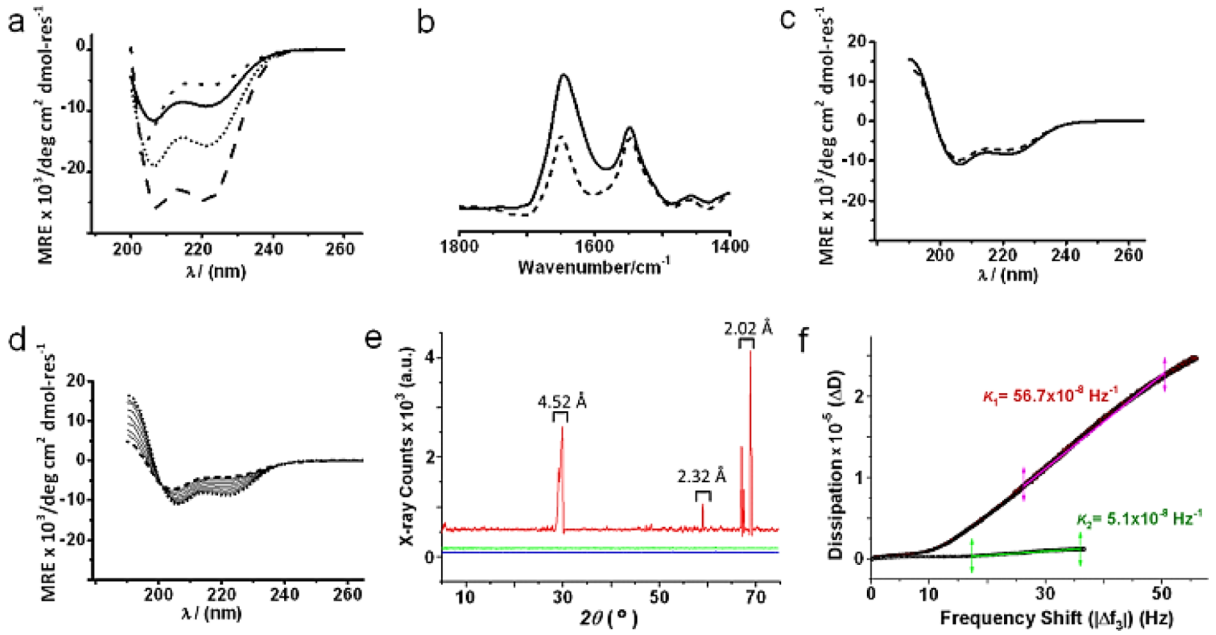

Figure 3. Peptide folding. (a) CD spectra for SaNet (solid line), D1−D2 (dashed line), D1 (dotted line), and D2 (space-dotted line). (b) FT-IR spectra for SaNet before (solid line) and after (dashed line) thermal denaturation. (c) CD spectra for SaNet before (solid line) and after (dashed line) thermal denaturation. (d) CD spectra following the thermal unfolding of SaNet: 10 °C (dotted line) and 90 °C (dashed line), with intervening spectra recorded every 10 °C (solid lines). Note the isodichroic point at ∼202 nm. (e) XRD patterns for SaNet (red), D2 (blue), and D1+D2 (green). (f) QCM-D ΔD versus $|\Delta f|$ plot. K_1 and K_2 correspond to the plot slopes for D2 and SaNet, respectively. Folding conditions: peptide (100 μM) incubated overnight at 20 °C in 10 mM MOPS buffer, pH 7.4.

interactions between the same domains (Figure 1). The stacking of SaNet blocks largely propagates through three-heptad interactions, which, unlike amyloid in cross-β spines,[21] is interrupted by one- and two-heptad interactions imposing directionally promiscuous assembly (Figure 1c). Such synergy in the SaNet assembly proved to be compatible with designed helical folding as confirmed by circular dichroism (CD) and Fourier transform infrared (FTIR) spectroscopies (Figure 3a,b). The helix content in the assembly was <25% and was lower than that for D1+D2 (35%) (Figure 3a).[22] The partial loss of helicity may be due to the triglycyl linkers contributing elements of disorder.[23] However, the thermal unfolding of the assembly revealed nearly complete reversibility of folding characteristic of a cooperatively folded structure (Figure 3c).[18,23] Thermal denaturation curves were approximately linear which is consistent with multiple helical assemblies and their partial fraying by the linkers (Figure S3a).

Additional support for this came from a clear isodichroic point at 202 nm, which provides a convenient measure of stability and cooperativity of helical assemblies (Figure 3d). This is a wavelength at which signal intensity remains the same despite perturbations caused by changing conditions, temperature, and is indicative of a two-state transition between helical and unfolded forms. CD spectra recorded for SaNet between 10 and 90 °C show a gradual transition from strongly helical spectra to those that are more characteristic of a random coil (Figure 3d). Further, the mixtures of individual and nonconstrained domains D1+D2 gave perfectly sigmoidal unfolding curves, with their first derivatives dominated by a single transition midpoint (T_M) of ∼55 °C (Figure S3b). The T_M values of resulting transitions correspond to the stability of the formed superhelix, the higher the more stable, whereas sigmoidal curves indicate cooperative transitions.

Interestingly, although D2 did not fold, CD spectra for D1 were partially helical (Figure 3a). However, the first derivatives of the thermal denaturation curves for D1 revealed overlapping transitions of nonspecific and possibly competing complexes (Figure S3c), while isodichroic points at 202 nm for both D1+D2 and D1 were less apparent suggesting equilibrium fluctuations between conformer populations (Figure S3d,e). As a result, D1 did not assemble (Figure S1e). Further evidence for the folding-mediated SaNet assembly was provided by X-ray diffraction (XRD) experiments using characteristic X-rays of λ = 2.2897 Å.[24,25]

This wavelength can obtain diffraction information from a depth of around 8 μm, which is compatible with the size and morphology of the assembled nets and with the sample preparation used for microscopy studies. XRD patterns for the nets revealed a dominating d-spacing of ∼4.52 Å (angle 2θ of 29−30°) corresponding perfectly to an average radius of lowest-energy coiled-coil dimers and was accompanied by a minor d-spacing of ∼2.32 Å (angle 2θ of 59.5°) consistent with the radius of an ideal α-helix.[26,27] Interestingly, average d-spacings of 2.02 Å derived from 68 to 69° peaks (2θ), which appear to be in good agreement with a radius typical of 3_{10} helices (1.9 Å), were also observed (Figure 3e).

These patterns suggest that long-range coiled-coil interactions provided by α-helical heptad overlaps may be accompanied by short and irregular para-helical regions (3_{10}).[28] In marked contrast, no periodicities were detected for D2 and D1+D2 (Figure 3e). The results in combination with the spectroscopy and microscopy data confirm near-crystalline periodicity for SaNet at the observed length scales. With the micro-nets assembled in solution showing no signs of cloudiness, gelation, or turbidity at any stage of the assembly at the concentrations used, it was reasonable to probe SaNet elongation kinetics at a solution-surface interface. With this in

dx.doi.org/10.1021/ja411325c | J. Am. Chem. Soc. 2014, 136, 7889−7898

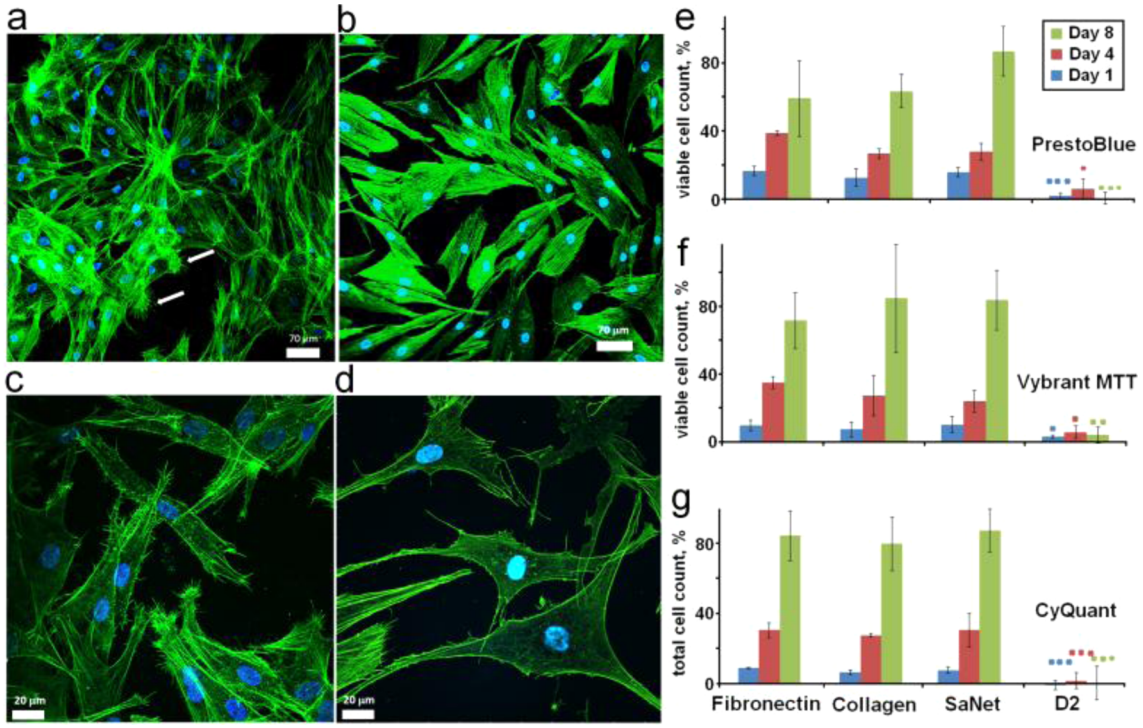

Figure 4. Cell growth and proliferation. Fluorescence micrographs of human dermal fibroblasts (HDFs) incubated on SaNet and fibronectin for a week (a,b) and for 24 h (c,d). Fluorescent stains Alexa-Fluor 488 phalloidin and 4′,6-diamidino-2-phenylindole highlight actin (green) and nuclear DNA (blue), respectively. In (a) white arrows point to visible filopodia protrusions. Total viable cell count (e,f) and total cell count (g) determined by PrestoBlue (e), Vybrant MTT (f), and CyQUANT (g) assays. Total number of cells on SaNet on day 8 was taken as 100% (SaNet highest for e and g) after subtracting the background adhesion (bare plastic). According to the analysis of variance (ANOVA) followed by a Fisher post-test for three independent experiments each done in triplicate for each test, cells grown on D2 substrates when compared to the other substrates had significantly lower numbers of metabolically active cells on (e) days 1 ($p < 0.001$),[a] 4 ($p < 0.05$), and 8 ($p < 0.001$); (f) on days 1 ($p < 0.05$), 4 ($p < 0.05$), and 8 ($p < 0.01$); and (g) significantly lower total numbers of cells on days 1 ($p < 0.001$),[a] 4 ($p < 0.001$), and 8 ($p < 0.001$). Significant differences are represented with * for $p < 0.05$, ** for $p < 0.01$, and *** for $p < 0.001$. [a]Other post-tests used (Scheffe, Tukey, Bonholm, Sidakaholm, Bonferroni, and Sidak) returned similar values within $p < 0.01$–0.001 ranges for given pairs of data sets. Incubation conditions: 50 μL of SaNet (464 μg/mL), fibronectin, and collagen (500 μg/mL).

mind, we performed quartz crystal microbalance with dissipation (QCM-D) monitoring in real time.[29,30] The measurements done at constant peptide concentrations and flow rates of peptide solutions allowed for the continuous monitoring of the SaNet assembly as a linear function of the material mass deposited on the crystal surface.[30] Here plotting changes in dissipation (ΔD) versus resonance frequency changes (Δf) provides an estimate of how new added mass affects the structure on the surface (Figures 3f and S2b). The slope of the plot is given by K, which is indicative of structure formation and kinetics during adsorption. A small value of K indicates the formation of a structured and rigid layer, which is in contrast to dissipated layer formation characterized by high K values.[31] The returned K_2(SaNet) values were an order of magnitude smaller when compared to K_1(D2), which is consistent with the suggestions that SaNet assembled into highly elongated fibrillar structures[30] and that D2 nonspecifically precipitated, forming a loosely bonded viscous layer.[29,31] Further, while D2 precipitated continuously, as expected for a nonequilibrating system, the assembled SaNet reached equilibrium with monomers in solution after the first 3–4 h, with only additive changes in Δf after (Figures 3f and S2b).[30] These results fully support a specific self-assembly process driven by minimized ΔG and are in good agreement with the folding and assembly data.

Differential Cell Adhesion and Proliferation. Collectively, the assembly characterization data confirmed the generation of micrometer-spanning peptide nets as designed. Because their dimensions and relatively homogeneous morphology were remarkably similar to those of native matrices the nets were tested as substrates for cell adhesion and proliferation, which were visualized by fluorescence microscopy (Figure 4a–d) and were monitored and quantified using three different cell proliferation assays (Figure 4e–g). Human dermal fibroblasts (HDFs) were seeded on five different substrates:- bare plastic, taken as a background; substrates coated with SaNet and D2, as a negative nonassembling peptide control; and collagen and fibronectin substrates used as positive fibrillar and matrix protein controls, respectively (Figure 4). PrestoBlue and Vybrant MTT cell proliferation and viability assays, which are quantitative chemical and enzymatic redox indicators of metabolically active cells, revealed that SaNet-coated substrates strongly promoted cell adhesion and proliferation, with cells remaining viable over a week (Figure 4e,f). Similar results were obtained by the CyQUANT cell assay (Figure 4g), which does not depend on the metabolic activity of cells or potential factors that can influence its measurement, but provide a direct measure of total cell numbers based on the total nucleic acid content. As seen in Figure 4, all three tests gave comparable values, expressed as the percentage of total cells (CyQUANT) and total cells that are viable (PrestoBlue and Vybrant MTT),

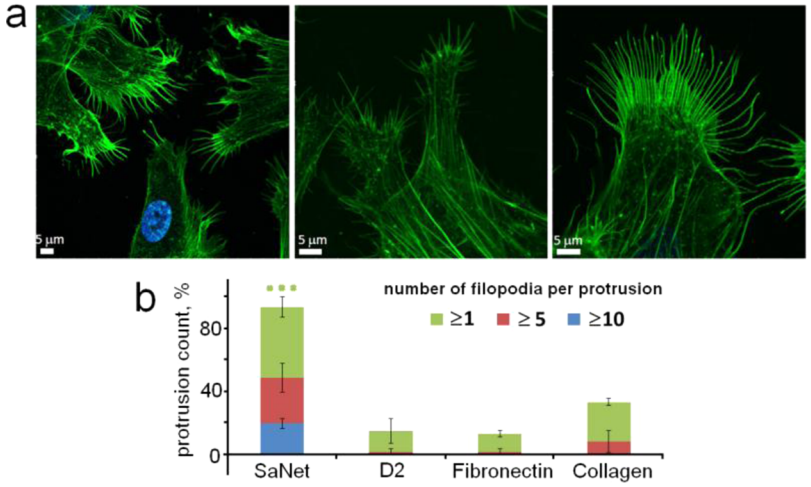

Figure 5. Filopodia-rich protrusions on SaNet. (a) Fluorescence microscopy images of filopodia protrusions on cells grown for 24 h. (b) Total counts of protrusions with filopodia for each substrate are given in percentage derived from the actual number of filopodia-rich protrusions (≥1, ≥5, or ≥10) divided by the total number of protrusions (≥1) after subtracting the background number (bare plastic). Protrusions with ≥10 filopodia were observed only for SaNet. According to ANOVA followed by a Fisher post-test for three independent experiments each done in triplicate for each test, cells grown on SaNet had significantly ($p < 0.001$) higher numbers of filopodia in comparison to any of the other substrates.

for fibronectin, collagen, and SaNet coatings with same cell proliferation trends (days 1, 4, and 8) (Figures 4e–g and S4). In contrast, all three tests detected only negligible cellular responses for D2 substrates (Figure 4e–g). It should be noted here that in contrast to collagen and fibronectin SaNet lacks known cell recognition motifs (e.g., RGD, YIGSR, IKVAV). This deficiency together with the negligible activity of D2, which is chemically identical to SaNet, suggests that in the absence of established ligands the unique architecture of the nets may contribute to cell–net interactions. In this light, the most notable differences were observed in cell behavior for SaNet substrates which revealed brushed filopodia protrusions and, at early stages of cell proliferation, seemingly smaller cells (Figures 4a,c and S4). However, the effect of reduced cell sizes was not ubiquitous for SaNet samples, unlike filopodia protrusions, which were abundant. Filopodia formation on SaNet substrates was already apparent within the first hours of cell adhesion (1 and 5 h), while cell spread areas were comparable with those for collagen and fibronectin substrates (Figures 5a, S5, and S6). Further, the presence of EDTA, which is used to block cation-mediated integrin function, had no effect on cell adhesion to SaNet substrates, while adhesion to fibronectin and collagen was almost completely inhibited (Figures S5 and S6c). Concomitantly, filopodia formation on SaNet substrates was equally apparent in the presence of EDTA (Figure S5). These findings, combined with the negligible activity of the D2 subsequence (Table S1, Figures S1 and S2) for both short- and long-term adhesions (Figures S5 and S6), imply that an integrin-independent component of cell anchorage capable of recognizing the SaNet architecture may promote cell–net interactions. The filopodia protrusions, observed for SaNet substrates irrespective of the applied adhesion conditions, were reminiscent of actin-supported growth cones[32] and were most evident at mobile edges of the cells (Figures 4c, 5a, S5, and S6). Cells incubated on SaNet from over a day to a week tended to weave into intricate cellular networks—a notable effect which was not observed for the other substrates (Figures 4 and S4). Given that filopodia are characteristic of transient adhesions of actively migrating cells and help cells probe their substratum and environmental cues,[33] the enhanced filopodia formation suggests enhanced cellular responses to the physical features of the SaNet matrix (Figures 4 a,c, 5a, and S4).[34] None of the other substrates used, and notably fibrous collagen, showed these or similar effects, which, to the best of our knowledge, have not been reported for any other mimetic system. Therefore, the observed behavior could be attributed to the unique architecture of the SaNet matrix. Indeed, while the micrometer-spanning nets can sustain cell proliferation and viability (Figure 4), specific elements of their morphology appear to elicit locally enhanced responses of individual cells (through filopodia formation) starting from initial attachment and developing over a week into distinctive proliferation patterns (Figures 4a,c, 5a, and S4–S6).[33,34]

Comparative impedance measurements using cell–electrode interfaces,[35] which help evaluate changes in effective impedance (resistance) to applied alternating current, provided further support for different cell proliferation patterns that were measured continuously in real time.[36] Typically, cell attachments to electrode surfaces give impedance increases, whereas changes in cell morphology (cell rounding-up and detachment) cause impedance drops. Resistance traces that can correspond to different events including changes in cellular morphology, patterning and growth rates were recorded as a function of time.[35,36] Cells were seeded in a serum-depleted medium to avoid interferences by serum, which can modulate same signaling pathways for cell adhesion. Impedance for fibronectin substrates increased sharply compared with that of collagen and SaNet substrates (Figure S7a), which was likely due to the nonspecific sedimentation of HDFs on the electrodes, which was also apparent for bare substrates used as controls.[37] Lower initial impedance values recorded for collagen and SaNet coatings may suggest a delayed or more matrix-directed mechanism of cell adhesion.

Indeed, after the first 8 h of initial attachment and spreading a lag phase showing relatively stabilized patterns for all substrates followed (Figure S7a). The second medium inoculation was followed by steady decays in resistance curves for fibronectin and bare substrates up to the point of a next cell doubling (40–50 h), whereupon no substantial changes in impedance were observed. In contrast, a gradually ascending

dx.doi.org/10.1021/ja411325c | J. Am. Chem. Soc. 2014, 136, 7889–7898

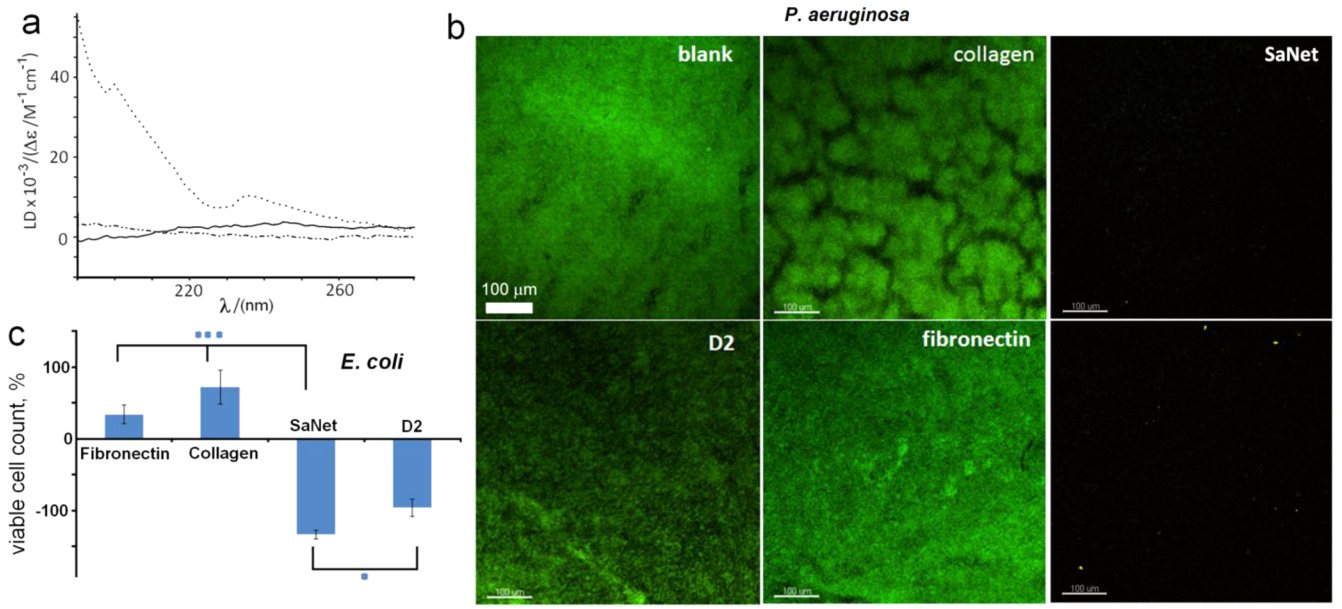

Figure 6. Membrane and bacterial cell interactions. (a) LD spectra for assembled SaNet in 10 mM phosphate buffer (solid line) and in the presence of mammalian (dash-dotted line) and microbial (dotted line) mimetic membranes. Folding conditions: lipid-peptide ratio 100:1 (30 μM peptide), 20 °C in 10 mM phosphate buffer, pH 7.4. (b) Fluorescence micrographs of *P. aeruginosa* after 16-h incubations on different substrates. Live/dead staining used to label live (green) and dead (red) bacteria. (c) total viable cell counts, determined by PrestoBlue, for *E. coli* colonization are given in percentage after subtracting the background adhesion (bare plastic), which was taken as 100%. The viability of cells grown on SaNet is significantly lower in comparison to fibronectin and collagen ($p < 0.001$) and to D2 ($p < 0.01$) according to ANOVA followed by a Fisher post-test for three independent experiments each done in triplicate for each test.

phase in impedance was recorded for fibrillar substrates, SaNet and collagen, suggesting comparable cellular responses (Figure S7a).

Because SaNet does not contain established cell recognition motifs the cumulative basis of cell responses to the nets may be different from that for collagen and fibronectin coatings. Equally importantly, cell responses to SaNet observed in all tests cannot be mediated by the binding of the nets to cellular membranes. Indeed, linear dichroism (LD) spectroscopy, which gives a straightforward probe of relative orientation of peptide binding in membranes,[38] revealed that SaNet did not specifically orient on mammalian mimetic membranes (zwitterionic unilamellar vesicles), suggesting that no interactions occurred.[39] In marked contrast, LD spectra recorded in the presence of bacterial mimetic membranes (anionic unilamellar vesicles) were characteristic of the on-surface orientation of SaNet helices with typical minima at 195−200 and 222−225 nm and a maximum at 205−210 nm (Figure 6a).[38]

These indicate that SaNet, through predominantly cationic domains, interacts with the anionic membranes and aligns parallel to their surfaces. This is important for two reasons. First, it implies that SaNet can elicit differential membrane responses discriminating the proliferation of one cell class from another. Cell proliferation supports multicellular living and is essential for tissue organization. However, it is not limited to eukaryotes. A prominent example is bacterial colonization and biofilm formation—a multicellular phenomenon implicated in a variety of infectious events that compromise normal tissue development and healing.[40] Strong bacterial adhesion, which can occur under 1 h,[41] can rapidly mature into biofilms on surfaces, which unless rendered antimicrobial remain attractive substrates for persistent bacterial colonization. Existing attempts to deter bacterial adhesion and biofilm formation include physical[42] and chemical[43] surface modifications and the use of polymeric hydrogels,[44] but these are specialist antimicrobial strategies that are not necessarily supportive of primary cell proliferation and may not be readily tailored for it. Similarly, inert and hydrophobic polymeric films assembled or covalently attached to solid substrates (gold, silicone) can elicit long-term (over 24 h) resistance to bacterial adhesion.[45−49] However, such surfaces are not necessarily differential as they are typically designed to resist the adsorption of proteins as well as the adhesion of mammalian and bacterial cells.[45−49] Second, which is directly relevant to the first point, SaNet design is intrinsically, albeit moderately, antimicrobial. The split 2+1 pattern of the SaNet block provides cationic two-heptad stretches, D2, that are meant to exhibit weakly antimicrobial activities,[50] which become amplified and apparent in the matrix (Figure 1d). This should make the matrix responsive to local bacterial adhesion, and more to individual cells rather than to the bulk bacterial culture. Individual D2 domains are too short to span or porate membranes,[39] but may be able to resist bacterial colonization as a coating on the surface. However, it is in the assembled matrix, in which they are prefolded to cover every third nanometer and at least 50% of its solvent exposed area, where their activity becomes most pronounced. A small fraction of a higher order fiber (Figure 2c) is equal to the size of a bacterial cell (<2 μm), which upon adhering on to the matrix can compete for cationic D2 domains.[51]

The affinity of these localized cationic domains to bacterial membranes is competitively higher than that for their complementary anionic domains, which is supported by LD experiments showing that SaNet responds only to the bacterial membrane mimetics adopting a specific orientation, which in turn can be achieved only through strong binding.[38,39] The continuous arrangement of the domains can thus be viewed as an antimicrobial "carpet" potentially resistant to bacterial adhesion and colonization.[39,51]

dx.doi.org/10.1021/ja411325c | J. Am. Chem. Soc. 2014, 136, 7889−7898

Consistent with this, SaNet substrates were found to resist colonization by *E. coli* and *P. aeruginosa* from the first hours that are critical for bacterial adhesion.[41,43] Quantitatively stronger responses were detected for SaNet over 16 h when compared with D2 (Figures 6b,c and S8). Similarly, the adhesion of *B. subtilis*, which tends to form less adherent floating pellicles, was inhibited by the SaNet substrates only (Figure S8). For all the tested bacteria adhesion-resistant effects of the nets were evident when compared to bacteria-fouled control coatings (Figures 6b and S8). Furthermore, impedance for SaNet remained in a negative phase with no signs of positive recovery over 15 h (Figure S7b).[52] In contrast, the natural substrates used in the study (fibronectin and collagen) did not resist bacterial colonization (Figures 6b,c, S7b, and S8). The resistance effect was particularly evident for SaNet substrates for long-term (over 24 h)[43,46] colonization (Figure S9). The substrates incubated with *P. aeruginosa* resisted bacterial adhesion for 4 days (96 h). Within the next 4 days, 4−8-day incubations, live bacteria were detected suggesting gradually increasing colonization (Figure S9). For day 10 (240 h) bacterial adhesions were comparable to those of control samples for 16 h. The gradual colonization observed as a function of time indicates that bacterial adhesion is prevented through resistance rather than a killing mechanism.[43] Consistent with this conclusion, microdilution assays, which gave quantified bacterial numbers in the presence of the SaNet peptide, showed negligible antimicrobial and hemolytic activities (Table S2).

The results provide complementary evidence for that the assembled SaNet is resistant to bacterial colonization over similar and in some cases substantially longer periods of time when compared to polymeric and peptoid surfaces reported by others.[43,45−49,53] However, the primary advantage for using SaNet nets is that they readily assemble from a single peptide and can be deposited as a coating without requirements for specialist chemistry or used in solution as a scaffold. The nets emulate the native extracellular matrices, but unlike these matrices and unlike other reported coatings, they support differential responses to cell adhesion—enhanced mammalian cell attachment and proliferation, and enhanced resistance to bacterial colonization—and do this at the native submillimeter length scales.

CONCLUSION

We have introduced a single-peptide self-assembly topology, which adopts a helical type of folding, stable and reversible, and enables the assembly of fibrous matrices, microscopic and biologically differential. The described SaNet is a synthetic approximation of the native extracellular matrices, which shares key physicochemical characteristics of the native systems including nanoscale order, hyper branched and knotted morphology and high persistence length of fibrillar structures. All these properties contribute to the formation of intricate fibrous networks that span nano- to sub-millimeter dimensions thereby allowing for the continuous expression of unique biofunctional characteristics programmed in the sequence, i.e., antimicrobial carpets and filopodia-recognized adhesion points. SaNet is the first synthetic topology, to our knowledge, that generates microscopic knotted matrices whose biological performance, scaffold support for mammalian cell proliferation and resistance against bacterial colonization, correlates with their morphological and chemical properties promoting thus an architectural model for differential extracellular matrices.

Given that the time period of several hours to a week, employed in this study, is deemed sufficient for mammalian cells to produce their own matrix and that deterrence of bacterial colonization is most critical during the first hours and days of tissue restoration,[1,7,11,40] the demonstrated differential impact of the matrix on cell adhesion and proliferation holds promise for biomedical applications. A particular application type would be determined by the nature of the cellular environment required to accommodate the described nets. SaNet as well as control matrices (collagen) were assembled in solution (3D environment) and if used as such can serve as a biodegradable scaffold once proven to be efficient in 3D cell culture. When deposited on a solid surface, which is a 2D environment, the application focus for the nets would change to a biodegradable coating, for which cell adhesion (mammalian and microbial) is the main functional determinant.

MATERIALS AND METHODS

Peptide Synthesis. All peptides (Table S1) were assembled on a Liberty-1 microwave peptide synthesizer (CEM Corp.) using solid-phase Fmoc/tBu protocols and HBTU/DIPEA as coupling reagents. Allyl-based orthogonal protocols were used for cyclization on resin. Rink amide 4-methylbenzhydrylamine resin was used throughout. Fmoc-Glu(OH)-OAll was used as a C-terminal residue attached via its γ-carboxyl to assemble and cyclize the SaNet peptide. Upon cleavage and deprotection (95% TFA, 2.5% TIS, 2.5% water) this Glu was converted into Gln. The identities of the peptides were confirmed by analytical RP-HPLC and MALDI-TOF.

MS $[M + H]^+$: SaNet, m/z 4644.5 (calc), 4645.8 (obs); D1, m/z 2186.6 (calc), 2187.3 (obs); D2, m/z 2184.7 (calc), 2186.1 (obs). $[M + Na]^+$ were also observed.

High-Performance Liquid Chromatography. Analytical and semipreparative gradient RP-HPLC was performed on a JASCO HPLC system using Vydac C18 analytical (5 μm) and semipreparative (5 μm) columns. Both analytical and semipreparative runs used a 10−60% B gradient over 50 min at 1 mL/min and 4.7 mL/min respectively with detection at 230 and 220 nm (buffer A, 5% and buffer B, 95% aqueous CH_3CN, 0.1% TFA).

Circular and Linear Dichroism Spectroscopy. CD spectra were recorded on an Applied Photosystem Chirascan spectropolarimeter fitted with a Peltier temperature controller. All measurements were taken in ellipticities in mdeg and after baseline correction were converted to mean residue ellipticity (MRE; deg cm^2 dmol res^{-1}) by normalizing for the concentration of peptide bonds and cuvette path length. Aqueous peptide solutions (300 μL, 100 μM in each peptide unless stated otherwise) were prepared in filtered (0.22 μm) 10 mM MOPS or phosphate buffer, pH 7.4. To calculate the percent α-helix, the equation, $-100([q]_{222} + 3000)/33\,000)$, was used.[22] Solution-phase flow LD spectra were recorded on a Jasco-810 spectropolarimeter using a photoelastic modulator 1/2 wave plate, and a microvolume quartz cuvette flow cell with ∼0.25 mm annular gap and quartz capillaries (all from Kromatec Ltd., UK). Molecular alignment was achieved through the constant flow of the sample solution between two coaxial cylinders−a stationary quartz rod and a rotating cylindrical capillary. LD spectra were acquired with laminar flow obtained by maintaining the rotation speed at 3000 rpm and processed by subtracting nonrotating baseline spectra. LD spectra recorded in the presence of synthetic membranes were prepared at a lipid:peptide molar ratio of 100:1 (3 mM total lipid, 30 μM peptide).

FTIR Spectroscopy. All FTIR spectra were collected using a Tensor-37 series FTIR spectrophotometer with a BioATR II unit (Bruker Optics, UK) as the sampling platform with a photovoltaic mercury cadmium telluride (MCT) detector and a Bruker Optics workstation equipped with OPUS software. Low-volume (20 μL) peptide samples (100 μM, 10 mM MOPS, pH 7.4) were placed in a circular sampling area of radius 2 mm with path length of 6 μm. This multireflection ATR accessory is based on a dual-crystal technology, which has an upper silicon crystal and a hemispherical zinc selenide

(ZnSe) lower crystal that does not come into contact with the sample. The temperature of the samples was maintained at 20 °C using a Peltier apparatus. All FTIR spectra were collected with resolution of 4 cm^{-1}, scanner velocity of 20 kHz, 256 scans, phase resolution of 32, and zero filling factor of 4.

Substrate Preparation and Visualization. The 200 μL samples (100 μM in each peptide or as stated otherwise) were incubated overnight in 10 mM MOPS or phosphate buffer, pH 7.4, 20 °C, after which 50 μL peptide solutions were mounted onto an appropriate substrate (see corresponding sections for microscopy, cell assays, bacterial colonization, and impedance measurements) and buffer excess was removed by blotting paper. Similarly, 50 μL of protein solutions (500 μg/mL) were used to prepare fibronectin and collagen coated substrates.

Atomic Force Microscopy. For AFM imaging a drop (5−10 μL) of the pre-incubated 100 μM solution of peptide in 10 mM MOPS (pH 7.4) was deposited on a clean silicon wafer and the buffer excess was removed by blotting paper. AFM images were obtained using an MFP-3D system (Asylum Research Ltd.). All measurements were carried out in tapping mode using PPP-NCHR-type cantilevers (Nanosensors). The cantilevers were coated with 30 nm thick aluminum on the detector side to enhance the reflectivity of the laser beam. A typical value of the cantilever resonance frequency was about 330 kHz and force constant 42 N/m. Images were processed using proprietary SPIP software, version 6.0.13. To minimize variations in the spatial resolution resulting from wear of the tip the cantilevers were changed regularly.

X-ray Diffraction. The XRD data were collected using Cr Kα radiation (λ = 2.2897 Å) on a Bruker D8 Discover diffractometer, with a D8 goniometer being set up in the Bragg−Brentano geometry using a θ−2θ drive. The incident X-ray beam was collimated using 1° slits. The diffracted beam was collected using a scintillation detector. The specimen wafers were held in place by a vacuum chuck and a 2θ scan was performed on each sample in turn from 5° to 80°. A step size of 0.02° 2θ was used with a count time per step of 0.4 s. After collection the background signal from the data was subtracted using the Bruker EVA program prior to converting the file into a Microsoft Excel format. All measurements were performed at room temperature with tube settings of 30 mA, 40 kV for all substrates prepared as for the AFM measurements.

Continuous-Flow QCM-D. QCM sensograms were recorded at 20 °C on a Q-Sense E1 instrument with a temperature-controlled fluid cell (Q-sense, Sweden). Peptide solutions (100 μM in 10 mM MOPS, pH 7.4) were passed over silicon dioxide coated quartz crystals (10 mm in diameter), with a fundamental frequency of about 5 MHz crystals, to continuously monitor adsorption. Following an equilibration phase (zone I in Figure S2b) peptide solutions were run at a continuous flow rate of 5 μL/min (zone II, Figure S2b). Obtained data were analyzed using the proprietary Q-Tools software. The measurements were performed at several harmonics (n = 3, 5, 7, 9, 11, and 13). Δf and ΔD were fitted for the third overtone using the Q-Tools software. The first resonance is generally perturbed by edge effects caused by the crystal mount. The results are presented as changes in resonance frequency (Δf) and dissipation (ΔD) with time due to peptide adsorption on the crystal surfaces.

Lipid Vesicle Preparation. The lipids, 1,2-dilauroylphosphatidylcholine (DLPC) and 1,2-dilauroyl-*sn*-glycero-3-phospho-(1′-*rac*-glycerol) (DLPG), 75%/25% (w:w) used for liposome construction were from Avanti Polar Lipids. The lipids were weighted up, dissolved in chloroform−methanol (2:1, v:v), dried under a nitrogen stream, and placed under vacuum overnight. The resulting film was hydrated to 10 mg/mL total lipid concentration in 10 mM phosphate buffer, pH 7.4. The suspension was then extensively vortexed, sonicated (30 °C) and extruded (15 times) through polycarbonate filters (0.05 μm) using a hand-held extruder (Avanti Polar Lipids) to give a clear solution containing small unilamellar vesicles (SUV), which were analyzed (50 nm) by photon correlation spectroscopy following the resuspension of vesicles to a final concentration of 1 mg/mL.

Photon Correlation Spectroscopy. Dynamic light scattering batch measurements were carried out on a Zetasizer Nano (ZEN3600, Malvern Instruments, Worcestershire, UK), in a low volume (100 μL) disposable cuvette at 25 °C. No filtration of peptide samples was carried out before the measurements so that assembly populations remain unaffected. Hydrodynamic radii were obtained through the fitting of autocorrelation data to a single exponential function using the manufacture's software, Dispersion Technology Software (DTS version 5.10).

Cell Culture and Seeding. Human dermal fibroblasts (Invitrogen, UK) were maintained in Medium 106 supplemented with low serum growth supplement (2% v/v) and antibiotics (10 μg/mL gentamicin; 0.25 μg/mL amphotericin B) in 25 cm^3 culture flasks. The cells were incubated at 37 °C, 5% CO_2 and 95% air humidity. At 70−80% confluency, cells were washed with PBS to remove the unattached cells, and then adhered cells were trypsinized (trypsin/EDTA 0.025:0.01%) followed by trypsin neutralizer (all from Invitrogen, UK). The harvested cells (of passages 3−5) were seeded for subsequent cellular analysis. For cytoskeletal visualization Nunc LabTek chambered cover glass slides were used as substrates.

To evaluate the initial attachment and spreading of individual cells,[54] well-separated cells (zero cell−cell contact) at 1- and 5-h time points were seeded on the glass substrates coated with 50 μL of peptide (464 μg/mL) or protein (500 μg/mL) at a low-seeding density of 1×10^3 in the serum-free medium (Medium 106 only). For tests in the presence of EDTA, EDTA (10 mM, final concentration) was added 15 min before seeding the cells onto the substrates.[55]

For cell attachment (first hours) preceding cell viability and proliferation assays cells were seeded at a density of 4×10^3 in the serum-free medium on substrates (sterile 96 well plates) coated with 50 μL of peptide (464 μg/mL) or protein (500 μg/mL). The medium was then switched to the medium (Medium 106) supplemented with low serum growth supplement (2% v/v) for the long-term evaluations (proliferation).

Quantitative Cell Viability and Proliferation Assays. Cell proliferation rates and viability were determined by PrestoBlue, Vybrant MTT, and CyQUANT assays on days 1, 4, and 8 (all from Life Technologies, UK).

PrestoBlue Assay. PrestoBlue reagent is supplied as a 10× solution and added to each well by diluting (1×) in the serum-free culture medium. The cells were incubated for 30 min at 37 °C in 200 μL of the reagent. The fluorescence of each well was measured with a microplate reader (BMG Labtech, Germany), with 544 nm excitation and 590 nm emission filters. A standard calibration curves were generated by plotting measured fluorescence values versus cell numbers. A cell dilution series (500−50000 cells) was done by seeding cells on sterile 96-well plates with overnight incubation before each given time point.

Vybrant MTT Assay. For the colorimetric 3-(4,5-dimethylthiazol-2-yl)-2,5-diphenyltetrazolium bromide (MTT) cell proliferation assay, the cell medium was removed from each well at the set time points and washed with PBS followed by the addition of MTT solution (10 μL, 5 mg/mL in PBS) and serum-free fresh media (100 μL). Following 4 h incubations with the reagent at 37 °C, the resultant formazan crystals were dissolved in dimethyl sulfoxide (50 μL) according to the manufacture's protocol. The absorbance intensity was measured by a microplate reader at 540 nm with a reference wavelength at 640 nm. A standard calibration curves were generated by plotting measured absorbance values versus cell numbers. A cell dilution series (500−50000 cells) was done by seeding cells on sterile 96-well plates with overnight incubation before each given time point.

CyQUANT Assay. CyQUANT GR dye was prepared in a cell-lysis buffer (according to the manufacturer's protocols) prior to each experiment by diluting this stock solution (400×) into the buffer. After days 1, 4, and 8, the cells grown on the various substrates were washed gently in PBS and stored in a −70 °C freezer. At the same time, to generate calibration data, a cell pellet (1×10^6) prepared to provide a cell dilution series was also frozen. Cells grown on the substrates along with the cell pellet were thawed at 37 °C. CyQUANT GR dye in the lysis buffer was added (1 mL) to the pellet and the lysate was resuspended by brief vortexing. A cell dilution series (500−50000 cells) was created with the CyQUANT GR in cell lysis buffer in a final

volume of 200 μL. A standard calibration curve was generated by plotting measured fluorescence values versus cell numbers. To quantify cell numbers grown on the substrates, the same volume of the reagent was added to each well. All of the samples were dark-incubated for 10 min at room temperature. The fluorescence of each well was measured with the microplate reader, with 485 nm excitation and 520 nm emission filters.

Cytoskeletal and Filopodia Visualization. Actin staining was performed using Alexa-Fluor 488 conjugated to phalloidin (Life Technologies, UK), following 1-, 4-, and 8-day incubations, cells were rinsed with warm PBS (pH 7.4), fixed in 10% neutral buffered formalin solution (Sigma-Aldrich, UK) for 15 min at room temperature, washed with PBS and permeabilised using 0.1% Triton-X100 in PBS. Cells were then extensively washed in PBS and incubated for 30 min at room temperature with 10 μg/mL phalloidin in PBS. After post-stain washing with PBS, cells were mounted in ProLong Gold with 4′,6-diamidino-2-phenylindole (DAPI) (Life Technologies, UK) and imaged using an inverted confocal laser scanning microscope (CLSM) (FV-1000, Olympus). The counts given in Figure 5b are averages measured over 10 regions of 60× confocal micrographs. The number of adhered cells (seeded with no cell−cell contact) for each substrate was measured from 15 representative areas imaged after 1-h incubations. An average cell area was quantified after 5-h incubations of well-separated cells (25−30 cells on each substrate) using Fuji ImageJ software.

Bacterial Colonization. Bacterial inocula (*E. coli*, *P. aeruginosa*, and *B. subtilis*) were prepared in Mueller Hinton broth at A_{600} = 0.6, then diluted to 1:100 in the pre-warmed medium, and 50 μL of this dilution was added to each well of the coated Nunc LabTek chambered cover glass slides. Bacterial films formed after incubations over 16 h, 48 h, 4 days, 6 days, 8 days, and 10 days were analyzed using a Live/Dead BacLight bacterial viability stain kit (Molecular Probes, UK), and were visualized by a confocal laser scanning microscope (CLSM) (FV-1000, Olympus). Bacterial viability was quantitatively probed by using PrestoBlue reagent, as used for the cell viability and proliferation assay. *E. coli* was seeded at the same density as above in sterile bare and coated 96-well plates. After incubation at 37 °C (or 30 °C for *B. subtilis*), a bacterial film at a given time point formed on each substrate was carefully washed with 10 mM Tris-HCl buffer, pH 7, to remove bacteria remaining in suspension. To each well was added 200 μL of PrestoBlue reagent diluted in Mueller Hinton broth, which was then incubated for 30 min at 37 °C. The fluorescence of each well was measured using a microplate reader with 544 nm excitation and 590 nm emission filters (Figures 6, S8, and S9).

Statistical Analysis. Statistical analysis for all the analytical data was performed by OriginPro 8.5 using ANOVA followed by a Fisher post-test for three independent experiments each done in triplicate for each test. Other multiple-means comparisons tests (Bonferroni, Tukey, Sidak, Bonholm, Scheffe, and Sidakholm), with p values <0.05 considered significant, were also performed to allow comparison. The results are expressed as an average ± standard deviation.

Impedance-Based Cell Sensor Measurements. Impedance measurements were performed using an xCELLigence system according to the manufacturer's protocols (Roche, UK; ACEA Biosciences, USA). Each electrode array comprises 16 wells, each of which was first coated with assembled SaNet and protein solutions and background measurements were carried out prior to cell seeding. Cells (10^4 per well) cultured as described above were seeded on the precoated wells. The electrical impedance of each well was automatically recorded every 5 min for the first 24 h and then every 30 min until the end, and were normalized and expressed using the proprietary software as normalized cell index. Bacterial adhesions were measured every 5 min for over 15 h.

Minimum Inhibitory Concentrations Assay. Minimum inhibitory concentrations (MIC) were determined by broth microdilution on *P. aeruginosa* ATCC 27853, *E. coli* K12, *S. aureus* ATCC 25723, *M. luteus* NCIMB 13267, and *B. subtilis* ATCC 6633 according to the Clinical and Laboratory Standards Institute. Typically, 100 μL of (0.5−1) × 10^6 CFU per ml of each bacterium in Mueller Hinton broth was incubated in 96-well plates with 100 μL of serial two-fold dilutions of the peptides (final concentrations, 100−0 μM) at 37 °C (or 30 °C for *B. subtilis* and *M. luteus*) on a 3D orbital shaker. The absorbance was measured after peptide addition at 600 nm using a Victor 2 plate reader (Perkin-Elmer). Minimum inhibitory concentrations (MICs) were defined as the lowest peptide concentration showing growth inhibition after 24 h at 37 °C. All tests were done in triplicate.

Hemolysis Assay. Hemolysis was determined by incubating 10% (v/v) suspension of human erythrocytes with peptides. Erythrocytes were rinsed four times in 10 mM PBS, pH 7.2, by repeated centrifugation and resuspension (3 min, 3000g). Erythrocytes were incubated at room temperature for 1 h in either deionized water (fully hemolysed control), PBS or with peptide in PBS. After centrifugation at 10.000g for 5 min, the supernatant was separated from the pellet and the absorbance measured at 550 nm. Absorbance of the suspension treated with deionized water defined complete hemolysis. The values given in Table S1 correspond to concentrations needed to kill a half of the sample population (50% lysis of human erythrocytes) and are expressed as median lethal concentrations, LC_{50}. All tests were done in triplicate.

Confocal and Optical Microscopy. High-resolution confocal images were acquired using a confocal laser scanning microscope (LEXT OLS3100) equipped with 408 nm LD class 2 laser with 5−100× objective lenses giving a total magnification of 120−14400×. Images were processed using the proprietary software. Optical micrographs were acquired on an Olympus CX40 microscope connected with high resolution CCD camera using a magnification of 50× objective MPLN Plan Achromat lenses. No image processing was performed after image acquisition.

■ ASSOCIATED CONTENT

Supporting Information

Tables, Scheme and Figures as described in the text. This material is available free of charge via the Internet at http://pubs.acs.org.

■ AUTHOR INFORMATION

Corresponding Author

max.ryadnov@npl.co.uk

Author Contributions

[§]N.F. and A.B. contributed equally.

Notes

The authors declare no competing financial interest.

■ ACKNOWLEDGMENTS

We acknowledge funding from the UK's Department of Business, Innovation and Skills and the Strategic Research Programme of the National Physical Laboratory. We thank Tony Fry and Maud Seraffon for their help with the XRD measurements.

■ REFERENCES

(1) Huebsch, N.; Mooney, D. J. *Nature* **2009**, *462*, 426.

(2) Kopeček, J.; Yang, J. *Angew. Chem., Int. Ed.* **2012**, *51*, 7396.

(3) Papapostolou, D.; Smith, A. M.; Atkins, E. D. T.; Oliver, S. J.; Ryadnov, M. G.; Serpell, L. C.; Woolfson, D. N. *Proc. Natl. Acad. Sci. U.S.A.* **2007**, *104*, 10853.

(4) Ryadnov, M. G.; Woolfson, D. N. *Angew. Chem., Int. Ed.* **2003**, *42*, 3021.

(5) Brown, A. E.; Litvinov, R. I.; Discher, D. E.; Purohit, P. K.; Weisel, J. W. *Science* **2009**, *325*, 741.

(6) Ryadnov, M. G.; Woolfson, D. N. *J. Am. Chem. Soc.* **2005**, *127*, 12407.

(7) Luo, Z.; Zhang, S. *Chem. Soc. Rev.* **2012**, *41*, 4736.

(8) Mager, M. D.; LaPointe, V.; Stevens, M. M. *Nat. Chem.* **2011**, *3*, 582.

(9) Hirst, A. R.; Roy, S.; Arora, M.; Das, A. K.; Hodson, N.; Murray, P.; Marshall, S.; Javid, N.; Sefcik, J.; Boekhoven, J.; van Esch, J. H.; Santabarbara, S.; Hunt, N. T.; Ulijn, R. V. *Nat. Chem.* **2010**, *2*, 1089.
(10) O'Leary, L. E. R.; Fallas, J. A.; Bakota, E. L.; Kang, M. K.; Hartgerink, J. D. *Nat. Chem.* **2011**, *3*, 821.
(11) Stephanopoulos, N.; Ortony, J. H.; Stupp, S. I. *Acta Mater.* **2013**, *61*, 912.
(12) Seeman, N. C. *Annu. Rev. Biochem.* **2010**, *79*, 65.
(13) Yin, P.; Hariadi, R. F.; Sahu, S.; Choi, H. M. T.; Park, S. H.; LaBean, T. H.; Reif, J. H. *Science* **2008**, *321*, 824.
(14) Aldaye, F. A.; Senapedis, W. T.; Silver, P. A.; Way, J. C. *J. Am. Chem. Soc.* **2010**, *132*, 14727.
(15) Chu, H.; Pazgier, M.; Jung, G.; Nuccio, S. P.; Castillo, P. A.; de Jong, M. F.; Winter, M. G.; Winter, S. E.; Wehkamp, J.; Shen, B.; Salzman, N. H.; Underwood, M. A.; Tsolis, R. M.; Young, G. M.; Lu, W.; Lehrer, R. I.; Bäumler, A. J.; Bevins, C. L. *Science* **2012**, *337*, 477.
(16) Marsden, H. R.; Kros, A. *Angew. Chem., Int. Ed.* **2010**, *49*, 2988.
(17) Ryadnov, M. G.; Bella, A.; Timson, S.; Woolfson, D. N. *J. Am. Chem. Soc.* **2009**, *131*, 13240.
(18) Bella, A.; Ray, S.; Shaw, M.; Ryadnov, M. G. *Angew. Chem., Int. Ed.* **2012**, *51*, 428.
(19) Pomerantz, W. C.; Yuwono, V. M.; Drake, R.; Hartgerink, J. D.; Abbott, N. L.; Gellman, S. H. *J. Am. Chem. Soc.* **2011**, *133*, 13604.
(20) Corrigan, A. M.; Muller, C.; Krebs, M. R. *J. Am. Chem. Soc.* **2005**, *128*, 14740.
(21) Sawaya, M. R.; Sambashivan, S.; Nelson, R.; Ivanova, M. I.; Sievers, S. A.; Apostol, M. I.; Thompson, M. J.; Balbirnie, M.; Wiltzius, J. J.; McFarlane, H. T.; Madsen, A. Ø.; Riekel, C.; Eisenberg, D. *Nature* **2007**, *447*, 453.
(22) Morrisett, J. D.; Jackson, R. L.; Gotto, A. M., Jr. *Biochim. Biophys. Acta* **1977**, *472*, 93.
(23) Ryadnov, M. G.; Ceyhan, B.; Niemeyer, C. M.; Woolfson, D. N. *J. Am. Chem. Soc.* **2003**, *125*, 9388.
(24) Pichot, V.; Risse, B.; Schnell, F.; Mory, J.; Spitzer, D. *Sci. Rep.* **2013**, *3*, 2159.
(25) Han, T.-H.; Park, J.-S.; Oh, J.-K.; Kim, S. O. *J. Nanosci. Nanotechnol.* **2008**, *8*, 5547.
(26) O'Shea, E. K.; Klemm, J. D.; Kim, P. S.; Alber, T. *Science* **1991**, *254*, 539.
(27) Offer, G.; Sessions, R. *J. Mol. Biol.* **1995**, *249*, 967.
(28) Enkhbayar, P.; Hikichi, K.; Osaki, M.; Kretsinger, R. H.; Matsushima, N. *Proteins* **2006**, *64*, 691.
(29) Höök, F.; Rodahl, M.; Brzezinski, P.; Kasemo, B. *Langmuir* **1998**, *14*, 729.
(30) Buell, A. K.; Dobson, C. M.; Welland, M. E. *Methods Mol. Biol.* **2012**, *849*, 101.
(31) Paul, S.; Paul, D.; Basova, T.; Ray, A. K. *J. Phys. Chem. C* **2008**, *112*, 11822.
(32) Geraldo, S.; Gordon-Weeks, P. R. *J. Cell Sci.* **2009**, *122*, 3595.
(33) Schäfer, C.; Borm, B.; Born, S.; Möhl, C.; Eibl, E. M.; Hoffmann, B. *Exp. Cell Res.* **2009**, *315*, 1212.
(34) Discher, D. E.; Mooney, D. J.; Zandstra, P. W. *Science* **2009**, *324*, 1673.
(35) Balasubramanian, L.; Yip, K. P.; Hsu, T. H.; Lo, C. M. *Am. J. Physiol. Cell Physiol.* **2008**, *295*, C954.
(36) Giaever, I.; Keese, C. R. *Nature* **1993**, *366*, 591.
(37) Atienza, J. M.; Zhu, J.; Wang, X.; Xu, X.; Abassi, Y. *J. Biomol. Screen.* **2005**, *10*, 795.
(38) Hicks, M. R.; Kowalski, J.; Rodger, A. *Chem. Soc. Rev.* **2010**, *39*, 3380.
(39) Rakowska, P. D.; Jiang, H.; Ray, S.; Pyne, A.; Lamarre, B.; Carr, M.; Judge, P. J.; Ravi, J.; Gerling, U. I.; Koksch, B.; Martyna, G. J.; Hoogenboom, B. W.; Watts, A.; Crain, J.; Grovenor, C. R.; Ryadnov, M. G. *Proc. Natl. Acad. Sci. U.S.A.* **2013**, *110*, 8918.
(40) Hall-Stoodley, L.; Costerton, J. W.; Stoodley, P. *Nat. Rev. Microbiol.* **2004**, *2*, 95.
(41) Liang, M. N.; Smith, S. P.; Metallo, S. J.; Choi, I. S.; Prentiss, M.; Whitesides, G. M. *Proc. Natl. Acad. Sci. U.S.A.* **2000**, *97*, 13092.
(42) Hasan, J.; Crawford, R. J.; Ivanova, E. P. *Trends Biotechnol.* **2013**, *31*, 295.
(43) Hook, A. L.; Chang, C. Y.; Yang, J.; Luckett, J.; Cockayne, A.; Atkinson, S.; Mei, Y.; Bayston, R.; Irvine, D. J.; Langer, R.; Anderson, D. G.; Williams, P.; Davies, M. C.; Alexander, M. R. *Nat. Biotechnol.* **2012**, *30*, 868.
(44) Li, Y.; Fukushima, K.; Coady, D. J.; Engler, A. C.; Liu, S.; Huang, Y.; Cho, J. S.; Guo, Y.; Miller, L. S.; Tan, J. P.; Ee, P. L.; Fan, W.; Yang, Y. Y.; Hedrick, J. L. *Angew. Chem., Int. Ed.* **2013**, *52*, 674.
(45) Ostuni, E.; Chapman, R. G.; Liang, M. N.; Meluleni, G. P.; Pier, G.; Ingber, D. E.; Whitesides, G. M. *Langmuir* **2001**, *17*, 6336.
(46) Cheng, G.; Li, G.; Xue, H.; Chen, S.; Bryers, J. D.; Jiang, S. *Biomaterials* **2009**, *30*, 5234.
(47) Chapman, R. G.; Ostuni, E.; Liang, M. N.; Meluleni, G.; Kim, E.; Yan, L.; Pier, G.; Warren, H. S.; Whitesides, G. M. *Langmuir* **2001**, *17*, 1225.
(48) Luk, Y.-Y.; Kato, M.; Mrksich, M. *Langmuir* **2000**, *16*, 9604.
(49) Harder, P.; Grunze, M.; Dahint, R.; Whitesides, G. M.; Laibinis, P. E. *J. Phys. Chem. B* **1998**, *102*, 426.
(50) Salick, D. A.; Kretsinger, J. K.; Pochan, D. J.; Schneider, J. P. *J. Am. Chem. Soc.* **2007**, *129*, 14793.
(51) Shai, Y. *Biopolymers* **2012**, *66*, 236.
(52) Stallaert, W.; Dorn, J. F.; van der Westhuizen, E.; Audet, M.; Bouvier, M. *PloS One* **2007**, *7*, e29420.
(53) Statz, A. R.; Park, J. P.; Chongsiriwatana, N. P.; Barron, A. E.; Messersmith, P. B. *Biofouling* **2008**, *24*, 439.
(54) Grinnell, F.; Feld, M. K. *Cell* **1979**, *17*, 117−129.
(55) Jiang, H.; Grinnell, F. *Mol. Biol. Cell* **2005**, *16*, 5070−5076.